

The origin of interferometric effect involving surface plasmon polariton in scattering near-field scanning optical microscopy

Yan Li,¹ Nan Zhou,¹ Edward C. Kinzel,² Xifeng Ren,^{3,4} and Xianfan Xu^{1,*}

¹*School of Mechanical Engineering and Birck Nanotechnology Center, Purdue University, West Lafayette, Indiana 47907, USA*

²*Mechanical and Aerospace Engineering, Missouri University of Science and Technology, Rolla, Missouri 65409, USA*

³*Key Laboratory of Quantum Information, University of Science and Technology of China, Hefei, Anhui, 230026, China*

⁴*renxf@ustc.edu.cn*
**xxu@ecn.purdue.edu*

Abstract: Scattering near-field scanning optical microscopy (s-NSOM) has been developed to characterize optical near field with spatial resolution on the order of 10 nm. In this work we report investigation of the interferometric patterns commonly occurred in s-NSOM measurements. To reveal the origin of such interference patterns, a simple nanoslit is used. Comparing the measured result with a simplified analytical model as well as full-field numerical simulations, it is shown that the interference pattern is predominantly formed by the in-plane component of incidence light and surface plasmon polariton (SPP) launched by the nanoslit. This result helps to understand the responses of plasmonic nanostructures during s-NSOM measurements.

©2014 Optical Society of America

OCIS codes: (180.4243) Near-field microscopy; (310.6628) Subwavelength structures, nanostructures; (260.3160) Interference.

References and links

1. A. Bek, R. Vogelgesang, and K. Kern, "Apertureless scanning near field optical microscope with sub-10 nm resolution," *Rev. Sci. Instrum.* **77**(4), 043703 (2006).
2. E. Bründermann and M. Havenith, "SNIM: Scanning near-Field Infrared Microscopy," *Annu. Rep. Prog. Chem. Sect. C* **104**, 235–255 (2008).
3. M. Rang, A. C. Jones, F. Zhou, Z. Y. Li, B. J. Wiley, Y. Xia, and M. B. Raschke, "Optical near-field mapping of plasmonic nanoprisms," *Nano Lett.* **8**(10), 3357–3363 (2008).
4. T. Y. Cheng, H. H. Wang, S. H. Chang, J. Y. Chu, J. H. Lee, Y. L. Wang, and J. K. Wang, "Revealing local, enhanced optical field characteristics of Au nanoparticle arrays with 10 nm gap using scattering-type scanning near-field optical microscopy," *Phys. Chem. Chem. Phys.* **15**(12), 4275–4282 (2013).
5. W. Chen, A. Kirilyuk, A. Kimel, and T. Rasing, "Direct mapping of plasmonic coupling between a triangular gold island pair," *Appl. Phys. Lett.* **100**(16), 163111 (2012).
6. A. Hartschuh, "Tip-Enhanced Near-Field Optical Microscopy," *Angew. Chem. Int. Ed. Engl.* **47**(43), 8178–8191 (2008).
7. C. Neacsu, G. A. Reider, and M. B. Raschke, "Second-harmonic generation from nanoscopic metal tips: Symmetry selection rules for single asymmetric nanostructures," *Phys. Rev. B* **71**(20), 201402 (2005).
8. C. Neacsu, J. Dreyer, N. Behr, and M. B. Raschke, "Scanning-probe Raman spectroscopy with single-molecule sensitivity," *Phys. Rev. B* **73**(19), 193406 (2006).
9. F. Keilmann and R. Hillenbrand, "Near-field microscopy by elastic light scattering from a tip," *Philos Trans A Math Phys Eng Sci* **362**(1817), 787–805 (2004).
10. R. Bachelot, P. Gleyzes, and A. C. Boccara, "Near field optical microscopy by local perturbation of a diffraction spot," *Microsc. Microanal. Microstruct.* **5**(4-6), 389–397 (1994).
11. N. Ocelic, A. Huber, and R. Hillenbrand, "Pseudoheterodyne detection for background-free near-field spectroscopy," *Appl. Phys. Lett.* **89**(10), 101124 (2006).
12. S. Aubert, A. Bruyant, S. Blaize, R. Bachelot, G. Lerondel, S. Hudlet, and P. Royer, "Analysis of the interferometric effect of the background light in apertureless scanning near-field optical microscopy," *J. Opt. Soc. Am. B* **20**(10), 2117–2124 (2003).
13. A. Fragola, L. Aigouy, and C. Boccara, "Interference Effect in Apertureless Near-Field Fluorescence Imaging," *Appl. Opt.* **42**(34), 6880–6888 (2003).

14. P. Lalanne and J. P. Hugonin, "Interaction between optical nano-objects at metallo-dielectric interfaces," *Nat. Phys.* **2**(8), 551–556 (2006).
 15. P. Lalanne, J. P. Hugonin, and J. C. Rodier, "Approximate model for surface-plasmon generation at slit apertures," *J. Opt. Soc. Am. A* **23**(7), 1608–1615 (2006).
 16. L. Zhang, A. Kubo, L. Wang, H. Petek, and T. Seideman, "Imaging of surface plasmon polariton fields excited at a nanometer-scale slit," *Phys. Rev. B* **84**(24), 245442 (2011).
 17. B. Wang, L. Aigouy, E. Bourhis, J. Gierak, J.-P. Hugonin, and P. Lalanne, "Efficient generation of surface plasmon by single-nanoslit illumination under highly oblique incidence," *Appl. Phys. Lett.* **94**(1), 011114 (2009).
 18. K. G. Lee, H. W. Kihm, K. J. Ahn, J. S. Ahn, Y. D. Suh, C. Lienau, and D. S. Kim, "Vector field mapping of local polarization using gold nanoparticle functionalized tips: independence of the tip shape," *Opt. Express* **15**(23), 14993–15001 (2007).
 19. J. T. Krug, E. J. Sánchez, and X. S. Xie, "Design of near-field optical probes with optimal field enhancement by finite difference time domain electromagnetic simulation," *J. Chem. Phys.* **116**(24), 10895 (2002).
 20. Z. Fei, A. S. Rodin, G. O. Andreev, W. Bao, A. S. McLeod, M. Wagner, L. M. Zhang, Z. Zhao, M. Thiemens, G. Dominguez, M. M. Fogler, A. H. Castro Neto, C. N. Lau, F. Keilmann, and D. N. Basov, "Gate-tuning of graphene plasmons revealed by infrared nano-imaging," *Nature* **487**(7405), 82–85 (2012).
 21. A. Huber, N. Ocelic, D. Kazantsev, and R. Hillenbrand, "Near-Field Imaging of Mid-Infrared Surface Phonon Polariton Propagation," *Appl. Phys. Lett.* **87**(8), 081103 (2005).
-

1. Introduction

Apertureless or scattering near field scanning optical microscopy (ANSOM or s-NSOM) has been demonstrated to achieve optical resolution of the order of 10 nm [1,2]. This ability of high resolution optical imaging has been applied to investigate optical interactions beyond the diffraction limit, including material identification [2], characterization of optical devices [3–5], and nanoscale spectroscopy [6–8]. The key of high resolution imaging in s-NSOM is the sharp tip used for measurements. The s-NSOM tip under light illumination provides local field enhancement by acting as a nanoscale scattering light source with the advantage of wavelength independence [9].

In spite of the advantages of s-NSOM resolution, s-NSOM suffers from an intense background signal from the back-scattered light collected by the detector. The background signal is a result of reflected light from the probe shaft and sample surface. This background signal is overwhelming considering that the useful signal only originates from a small region of tip-sample interaction, which is of the order of tens of nanometers [9]. Several methods have been proposed to suppress the background, for instance, regulation of tip sample distance [10], high harmonic demodulation [2], and interferometric modulation [3,11]. These methods have been proven to be able to extract near-field signal from the background noise. Meanwhile, optical interferences are often observed in s-NSOM data after applying these background suppression methods. These interference patterns are generally explained as a result of interference between the field scattered by the s-NSOM tip and the back-scattered light from surface asperities [12,13].

In this work, we report a different mechanism of interference formation in s-NSOM measurements using both an analytical model and numerical simulations. The measurement is performed using an s-NSOM system applying the pseudo-heterodyne background suppression method [11]. We show that the observed interference fringes of a simple sample, a nanoslit, originate from the interaction between in-plane component of the incident light and surface plasmon polariton (SPP) launched by the nanoslit. This result will clarify the hybridization of optical fields in s-NSOM measurements, especially when studying plasmonic structures.

2. Experimental

The experiment is carried out using a home-made reflection type s-NSOM system. A schematic of the experimental setup is shown in Fig. 1. This s-NSOM setup is based on a commercial Atomic Force Microscopy (AFM) system CombiScope 1000 from AIST-NT. A diode laser with wavelength of 1,300 nm is used for optical lever feedback in AFM to avoid interfering with the measurements conducted in visible wavelength range. The excitation laser source is a 633 nm Helium-Neon (HeNe) laser. The laser beam is expanded and collimated to provide better focus and flatter wavefront. The polarization direction of the laser beam is adjusted using a $\frac{1}{2}$ waveplate. A Mitutoyo objective with numerical aperture of 0.42 is used to

focus the laser beam onto the apex of s-NSOM tip. A three-axis piezo scanner is used to mount this objective, and provides accurate control of laser focusing location. For s-NSOM measurement, the AFM is generally operated in the tapping mode, with the s-NSOM probe oscillating at its fundamental resonance frequency. The back-scattered light is collected by the same objective and directed to an avalanche photodiode detector (APD). An interferometric pseudo-heterodyne method is applied to suppress the background noise in the s-NSOM measurement [11]. This setup can essentially be viewed as a modified Michelson interferometer. The incident light is divided into two paths by a cube beam splitter. The path including the objective and AFM is referred as the measurement arm, while the other is the reference arm. The laser power going into the measurement arm is about 6 mW. The same amount of laser power goes into the reference arm, which is then reflected by a mirror mounted on a piezo actuator. The back-scattered light and the reflected reference light combine at the beam splitter. The APD detects the combined light and outputs the signal to a lock-in amplifier (HF2LI-MOD, Zurich Instruments). The mirror on the piezo actuator is oscillating at a frequency of 200 Hz, modulating the signal into sidebands of harmonics of the probe oscillating frequency ω_0 . The lock-in amplifier then demodulates the signals, conveying the results to the AFM controller for the purpose of mapping.

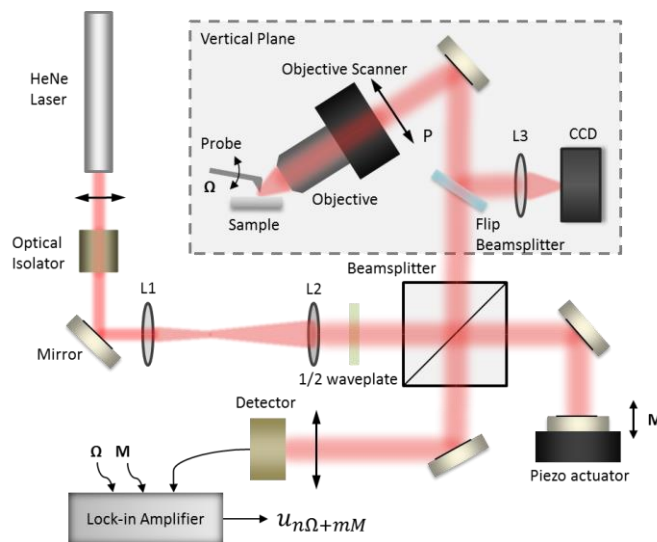


Fig. 1. Schematic of s-NSOM setup.

The sample used in this study is a 60 nm thick gold film coated on a glass substrate using an E-beam evaporator (CHA Industries). Nanoslits with width of 200 nm are fabricated using focused ion beam (FEI Nova 200 Dual Beam FIB/FEM) milling. Commercial AFM probes (ARROW-NCPT, NanoWorld) with platinum coating on the tip side are used for all the measurements. The nominal radius of the tip apex is 25 nm. Incidence beam comes in at an angle of 58° from surface normal before being focused by the objective.

With the use of this pseudo-heterodyne interferometric method, signals at the 1st sideband and 2nd sideband of $2\omega_0$ are obtained together with the corresponding topography. The near field amplitude and phase information is then recovered from these two signals [11]. Figure 2 shows an AFM topography image and optical images of the nanoslit. Looking down onto the sample in these images, the incident light radiates from the bottom toward the nanoslit. In Fig. 2(a), the normal direction of nanoslit is parallel (0°) to incident plane. Figures 2(b) and 2(c) are optical amplitude and phase images corresponding to the topography in Fig. 2(a). Figures 2(d) and 2(e) are optical amplitude images corresponding to nanoslit angles of 26° and 45° , respectively (oriented between the normal direction of nanoslit and the incident plane). The optical images show consistent results of different patterns on the two sides of the nanoslit:

distinct fringes appear on the lower part, the direction of the incoming laser beam, while no fringe or only slow intensity variation appears on the upper part of the nanoslit. All fringes are found to be parallel to the nanoslit. In addition, the envelope of optical phase fringes is found to be about $\pi/2$ ahead of the amplitude envelope, indicated by the white dashed lines in Fig. 2(b) and 2(c).

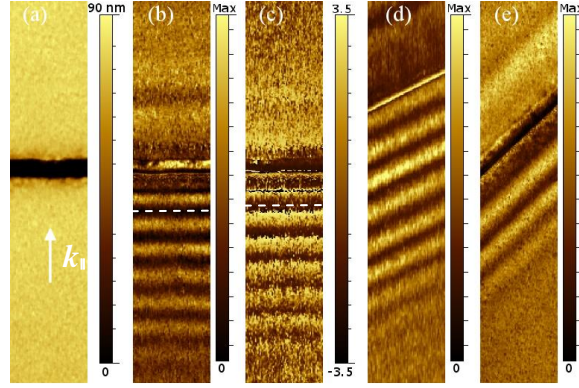


Fig. 2. Topography (a), s-NSOM amplitude (b), and phase (c) of nanoslit at orientations of 0° ; s-NSOM amplitude with nanoslit orientation at 26° (d) and 45° (e). Scan size is $1\ \mu\text{m}$ by $5\ \mu\text{m}$. k_{\parallel} in (a) is the in-plane component of incident light.

3. Analytical model and numerical simulations

We interpret the observed interference fringes as a result of interference between the SPP launched at the nanoslit and the in-plane component of the incident radiation. It is known that structures on a metal surface can excite surface plasmon polariton (SPP) under light illumination [14]. A simple structure such as nanoslit can have a high efficiency for SPP generation under oblique illumination [15]. This is a common situation for an s-NSOM setup with a side collection objective. The p -polarized excitation light can launch SPP on both sides of a nanoslit; then the SPPs propagate away from the nanoslit. The incident wave interferes with the two SPPs, forming fringes on both sides. This laser-SPP interaction can be described by an analytical model [16,17]. Due to the different propagation directions of the two SPPs with respect to the in-plane component of incident radiation, the interference periods are different on two sides of nanoslit, which can be described as:

$$\Lambda^- = \lambda_o \lambda_{SP} / (\lambda_o + \lambda_{SP} \cdot \sin(\theta) \cos(\varphi)) \quad (1)$$

$$\Lambda^+ = \lambda_o \lambda_{SP} / (\lambda_o - \lambda_{SP} \cdot \sin(\theta) \cos(\varphi)) \quad (2)$$

where λ_o in our case is 633 nm for the incident wavelength, λ_{SP} is the wavelength of SPP, θ is the angle of incidence with respect to the sample surface normal, and φ is the angle between normal direction of nanoslit and the incident plane. The permittivity of the gold film is measured using an ellipsometer to be $-10.789 + 1.902i$ at 633 nm. θ is fixed at 58° in our setup. Using these values, the periods Λ^- and Λ^+ are found from Eq. (1) and Eq. (2) to be 334 nm and $3.1\ \mu\text{m}$, respectively, when orientation of nanoslit is perpendicular to the plane of incidence ($\varphi = 0^\circ$). These two equations also indicate that when the orientation angle φ increases, the period of interference fringes increases, while the fringes will still be parallel to the orientation of nanoslit. For example, when $\varphi = 26^\circ$, the periods Λ^- and Λ^+ will be 349 nm and $2.2\ \mu\text{m}$ respectively; and when $\varphi = 45^\circ$, the periods Λ^- and Λ^+ will be 383 nm and $1.4\ \mu\text{m}$ respectively. Note the fringe spacings are identical for out of plane and in plane incident fields.

To further illustrate formation of interference, numerical simulations are performed using commercial frequency domain finite-element method (FEM) software (HFSS, Ansoft LLC).

The simulation model consists of a 60 nm thick Au film on top of a fused silica substrate ($n = 1.457$ at 633 nm). The nanoslit is 200 nm wide as in the experiment. A p -polarized Gaussian beam with a beam waist of $\omega_o = 2 \mu\text{m}$ is focused at the center of the nanoslit. The simulation results of the transverse electric field component E_z are shown in Fig. 3, which indicate different patterns formed on two sides of the nanoslit, in agreement with the analytical model and experimental observations. Here E_z is presented because s-NSOM is most sensitive to the vertical field component especially when a metal coated tip is used [18]. Three different orientations of nanoslit are simulated. The periods on the lower side of nanoslit are found to be 333 nm, 359 nm, and 408 nm for angles of 0° , 26° , and 45° , respectively. On the upper side, there is also intensity variation; however it is not sufficient to calculate the exact period (to be addressed more later). The fringe orientation also agrees with the model that the fringes are formed by the interference between SPPs and the in-plane component of the incident wave.

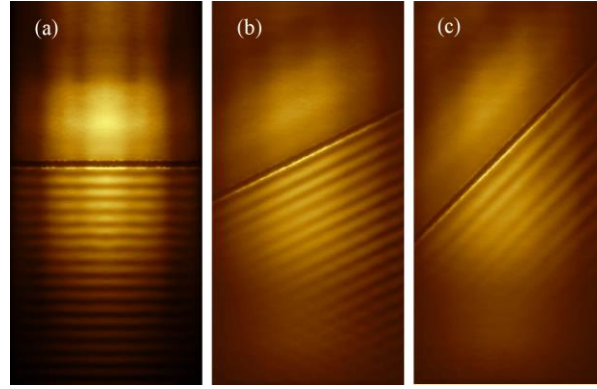


Fig. 3. Numerical simulations of a Gaussian beam radiating on the nanoslit with orientation of (a) 0° , (b) 26° , (c) 45° . Image size is $5 \mu\text{m}$ by $10 \mu\text{m}$.

To examine the measured phase information, we apply the same analytical model and express the electric field component E_z explicitly. The model computes the total field as the superposition of the incident field, its reflection, and the SPP launched by nanoslit. For a transverse magnetic (TM) mode plane wave incidence,

$$\mathbf{E} = \mathbf{E}_o \exp[j(\omega t - \mathbf{k}_o \cdot \mathbf{r})], \quad (3)$$

the E_z field can be expressed as,

$$E_z^-(x, z) = E_o \sin(\theta) \exp(-jk_{\parallel}x) [\exp(jk_{\perp}z) + r \exp(-jk_{\perp}z)] + A \exp(jk_{sp}x) \exp(-\gamma z), \quad \text{for } x < 0. \quad (4)$$

$k_{\parallel} = k_o \sin(\theta)$, $k_{\perp} = k_o \cos(\theta)$, r is the Fresnel reflection coefficient, $\gamma = (k_{sp}^2 - k_o^2)^{1/2}$, and $x = 0$ is at the center of the nanoslit. A is the relative amplitude of SPP with respect to the amplitude of the incident wave. Here it is determined to be $0.1 - 1i$ by matching both the interference contrast and the position of peaks of the measured amplitude result (Fig. 4(a)). A plot of the calculated E_z at $z = 0$, including both amplitude and phase, is presented in Fig. 4(b). In the plot, the near field phase (red curve) has the same periodicity as the near field amplitude (black curve), and the phase envelop has a lead of $\sim \pi/2$ relative to the amplitude envelop. These results are consistent with the measurement shown in Figs. 2(b), 2(c), and Fig. 4(a). A numerical simulation is also conducted using HFSS, using similar configuration but with an incident Gaussian beam. The simulated E_z in Fig. 4(c) shows the same conclusions as the measurement and the analytical calculation, i.e., there is a $\pi/2$ lead of the phase envelop. The differences in the details are mostly a result of different scenarios used in the three cases. The simplified analytical model assumes a plane wave illuminating the whole sample surface,

resulting in a much slower decay of interference than the other two plots. In the experiment, the laser beam is focused at the tip during sample scanning. While in the numerical simulation, the tip is absent and a Gaussian beam with a finite size is focused at the nanoslit center.

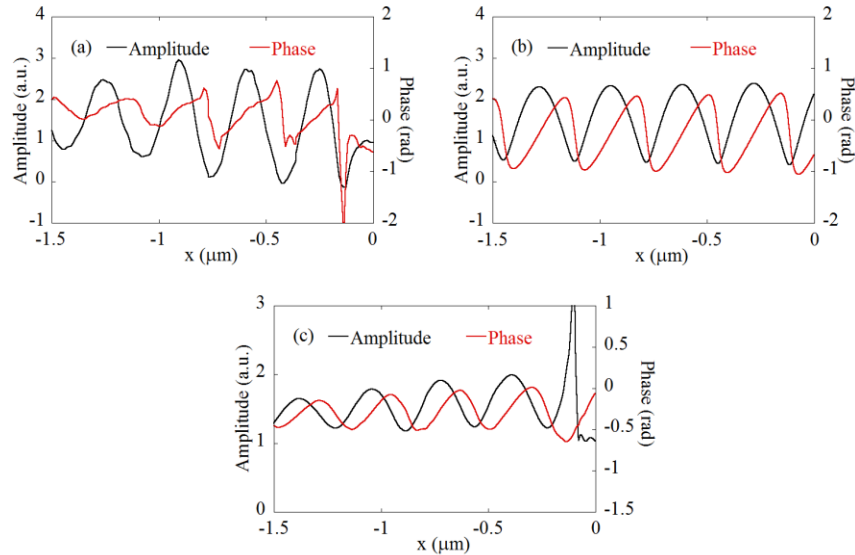


Fig. 4. (a) Line profiles of experiment amplitude and phase. (b) Amplitude and phase of E_z calculated from Eq. (4). (c) Amplitude and phase of E_z from numerical simulation.

4. Discussions

Both the analytical model and the numerical simulation indicate that the fringe spacing depends on the orientation of nanoslit due to the difference in the angle between propagation direction of excited SPP and the in-plane wave vector of incident wave, and the interference fringes are parallel to the nanoslit. These computed results agree well with the experimental data. Quantitatively, from the measured NSOM images shown in Fig. 2, we obtain fringe periods of 340 nm for 0° (Fig. 2(b)), 358 nm for 26° (Fig. 2(d)) and 367 nm for 45° (Fig. 2(e)). Applying the analytical model, the periods for these three angles are 334 nm, 349 nm, and 383 nm, respectively. Meanwhile the numerical simulation yields a result of 333 nm, 359 nm, and 408 nm, respectively. In general, the experimental results agree with the calculations. Deviations could come from a few factors, e.g., the analytical model assumes a plane wave illumination with a uniform wave front, while a focused Gaussian beam is used in the experiment, having wavevectors in many different directions. Also, the laser focusing position on the sample is constantly changing relative to the nanoslit since the sample is moved under the still tip during the scanning process. In addition, the existence of s-NSOM tip also has an effect on the interference pattern. Although we consider the effect from the tip to be minor (more to be discussed later), the presence of the s-NSOM tip may contribute to the discrepancy between the calculated and measured fringe spacing.

The analytical model predicts fringes with different periods existing on both sides of the nanoslit, whereas fringes appear predominantly on one side of the nanoslit in NSOM measurements. A main reason for this is, during the measurement, the laser focusing position is fixed at the static tip when the sample is moving. Due to the limited laser spot size, the larger fringe periods on the upper part of the nanoslit in Fig. 2 could not be captured experimentally.

The analytical model and the numerical simulation only include SPP generated by the nanoslit. However it is known that s-NSOM tip could provide field enhancement and launch

SPP as well [19]. For example, interference patterns have been observed in a graphene sample under infrared laser irradiation [20], which was explained as the interference between a SPP launched by tip and its reflection from the boundary of the graphene layer. In our measurement, the variation of fringe period at different nanoslit orientations and the very different fringes at two sides of nanoslit indicate that the interference between tip-launched SPP and slit-reflected SPP cannot be responsible for the formation of these fringes, otherwise the period of these fringes would be independent of the nanoslit orientation, and same fringes would appear on the two sides of nanoslit. We note that a similar phenomenon was reported on near-field imaging of mid-infrared surface phonon polariton (SPhP) [21]. The interference pattern observed in [21] was explained as the interference between the illuminating field and the launched SPhP. Applying Eq. (2), the calculated spacing of the interference is consistent with the measurement result in [21].

To further illustrate that the interference pattern is formed by SPP launched at the nanoslit, we carry out experiments under different focusing conditions. We move the focused laser spot away from the tip as shown in Fig. 5(a) for a distance of 0.5 μm . Note that during the scanning process, the sample moves to form the image, therefore the relative position between the focused laser spot and the tip does not change. At each of the three locations 1, 2, and 3 shown in Fig. 5(a), a corresponding near field image is obtained and shown in Fig. 5(c), 5(d), and 5(e), respectively. The center position 2 is determined by blocking the reference light and mapping the light intensity scattered by the tip using the objective scanner (Fig. 5(b)). The projection of probe in this image is marked with the dashed line and the incident light comes from the right side of the image. This map confirms the optical alignment at position 2. The

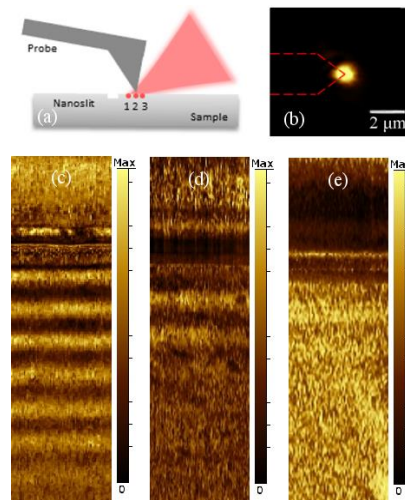


Fig. 5. (a) Illustration of the tip-sample interaction region with focused laser (separation between 1, 2, 3 is about 500 nm); (b) Image of focused laser spot by tip scattering; (c) s-NSOM image when laser focused at point 1; (d) s-NSOM image when laser focused at point 2; (e) s-NSOM image when laser focused at point 3. Image size of (c) (d) (e) is 1 μm by 3.5 μm .

NSOM images obtained at the three locations show a strong dependence on the focusing position. At position 1, where the focused laser spot is to the left of the tip apex and closer to the slit, the signal of the interference fringes is strongest, while at position 3 the laser spot is further from the slit, the fringe is weakest. This is another indication that the fringes are produced by the PP generated by the slit rather than the tip.

5. Conclusions

In conclusion, we investigated the formation of interference fringes in the s-NSOM measurement of a single nanoslit. Both amplitude and phase of the interference fringes were obtained, providing complete information of the measured optical near field components. The

observed spacing of interference fringes varies upon rotation of the nanoslit. It is shown that the fringes are formed due to the interference between the SPP generated by the nanoslit and the in-plane component of the incident laser beam, different than the mechanism reported in [20]. The nature of this interference pattern adds complexity to the s-NSOM images and needs to be taken into account in the interpretation of s-NSOM measurements, especially those of plasmonic nanostructures.

Acknowledgments

Supports to this work by the Defense Advanced Research Projects Agency (Grant No. N66001-08-1-2037), the National Science Foundation (Grant No. CMMI-1120577), and ASTC- the Advanced Storage Technology Consortium are gratefully acknowledged.